

www.acsnano.org

# Label-Free Ultrasensitive Detection of Abnormal Chiral Metabolites in Diabetes

Yaoran Liu,<sup>#</sup> Zilong Wu,<sup>#</sup> Pavana Siddhartha Kollipara, Richard Montellano, Kumar Sharma,\* and Yuebing Zheng\*



Cite This: ACS Nano 2021, 15, 6448-6456



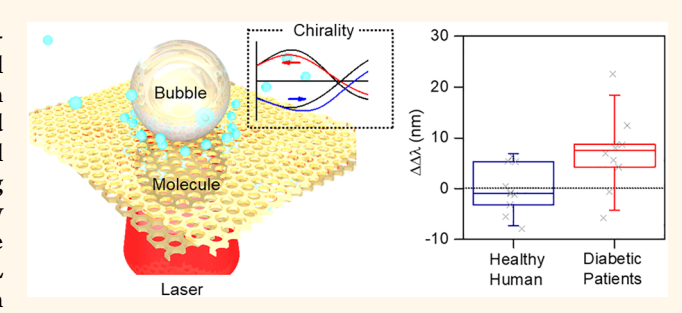
**ACCESS** 

III Metrics & More

Article Recommendations

Supporting Information

ABSTRACT: Homochirality is necessary for normal biochemical processes in humans. Abnormal amounts of chiral molecules in biofluids have been found in patients with diabetes. However, the detailed analysis of diabetes-related abnormal chirality in biofluids and its potential use for clinical applications have been hindered by the difficulty in detecting and monitoring the chiral changes in biofluids, due to their low molar mass and trace concentrations. Herein, we demonstrate the label-free detection of chiral molecules using only 10  $\mu$ L with  $10^7$ -fold enhancement in sensitivity compared with traditional plasmonic chiral metamaterials. The ultrahigh



sensitivity and low sample consumption were enabled by microbubble-induced rapid accumulation of biomolecules on plasmonic chiral sensors. We have applied our technique on mouse and human urine samples, uncovering the previously undetectable diabetes-induced abnormal dextrorotatory shift in chirality of urine metabolites. Furthermore, the accumulation-assisted plasmonic chiral sensing achieved a diagnostic accuracy of 84% on clinical urine samples from human patients. With the ultrahigh sensitivity, ultralow sample consumption, and fast response, our technique will benefit diabetes research and could be developed as point-of-care devices for first-line noninvasive screening and prognosis of prediabetes or diabetes and its complications.

KEYWORDS: chiral metamaterials, chiral metabolites, accumulation, diabetes, plasmonics

s building blocks of life, chiral molecules in human bodies are usually dominated by one of the enantiomers, showing homochirality, which is essential for proper biochemical reactions such as protein folding. An abnormal concentration of chiral molecules has been observed in human bodies with increasing age<sup>2,3</sup> and various chronic diseases, such as cancer, diabetes, kidney disease, and neurological disease, indicating the potential of applying chiral biomarkers as health indicators for diagnostic and prognostic applications.<sup>5,6</sup> In particular, elevated levels of many D-type metabolic molecules in urine have shown a strong correlation with diabetes mellitus. For example, urine is found to have an increased level of glucose, which is predominantly D-type in the human body, due to diabetes-induced glycosuria. A recent study found that patients with diabetes also have elevated urinary D-lactate as compared to controls.8 The discovery of such correlations between diabetes and an elevated level of chiral metabolic molecules indicates that monitoring the abnormal chiral changes of urine metabolites may offer a promising route toward noninvasive diabetes diagnosis and specific clinical therapy.

Measurement of chirality of urine metabolites has not been fully explored as a diagnostic method, hindering clinical development of chirality-based disease diagnosis and monitoring. In particular, establishing an accurate relationship between diabetes and chirality of metabolites in urine is crucial to improving knowledge on the pathological roles of chiral disorder. However, it remains greatly challenging to rapidly determine the chirality of urine metabolites with high accuracy. There are currently no available point-of-care devices that measure chiral molecules in clinical solution. Specifically, despite the ultrahigh sensitivity of high-performance liquid chromatography, gas chromatography, and capillary electrophoresis coupled to mass spectroscopy for chiral resolution of biomarkers, <sup>6,9</sup> such separation-based techniques demand a

Received: October 21, 2020 Accepted: March 16, 2021 Published: March 24, 2021





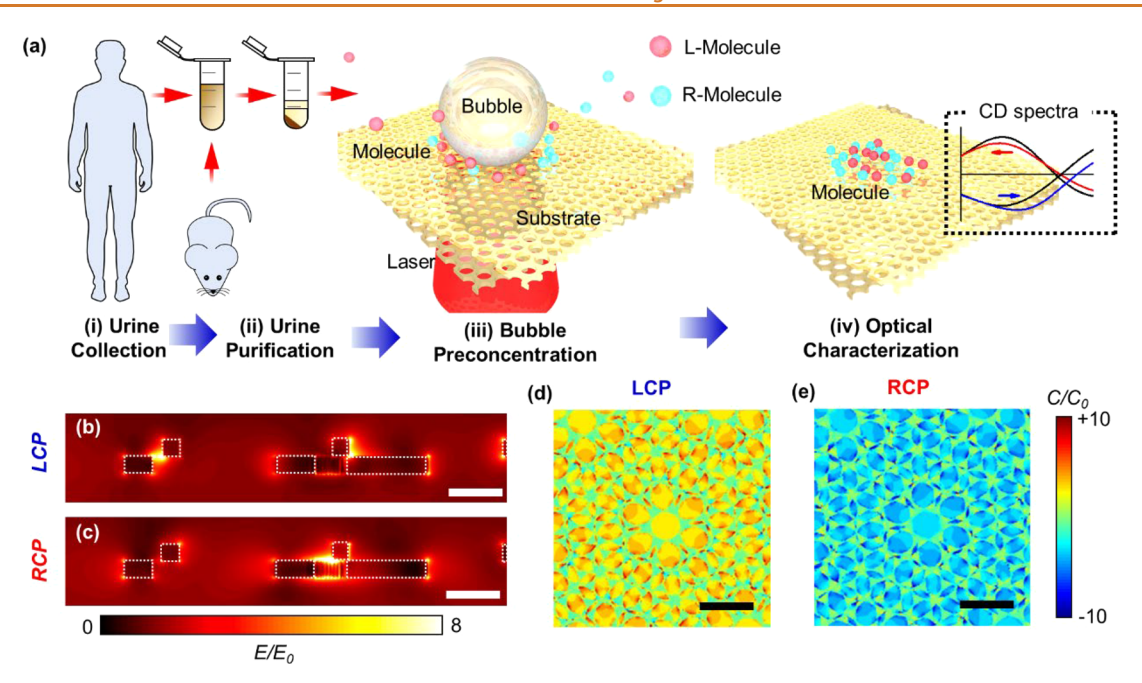


Figure 1. (a) Schematic illustrating the collection and purification of urine samples, and the microbubble-enabled accumulation of chiral metabolic molecules on MCMs for enhanced chiral sensing and diabetic detection via asymmetric spectral shifts. (b, c) Simulated distribution of electric field enhancement in an RH-MCM under (b) LCP and (c) RCP illumination at a wavelength of 675 nm. The scale bar is 100 nm. The white dotted lines mark the cross sections of the Au nanohole arrays in the MCMs. (d, e) Simulated distribution of local optical chirality at the center plane of the RH-MCM under (d) LCP and (e) RCP illuminations at a wavelength of 675 nm. The scale bars are  $1 \mu m$ .

molecule-exclusive chiral selector. The specific measurements of each chiral molecule reduce the ability to investigate the total chiral level and the effects of overall chiral balance in body solutions. Although the mass spectrometer has the capacity to separate chiral molecules, the slow processing speed, the high cost, and the demand for highly experienced operators limit the application of mass spectrometer-based techniques at point-of-care settings. 11 High-throughput chiral measurements have remained impractical for clinical trials or patient care. Chiroptical techniques such as circular dichroism (CD) spectrometers and polarimeters can overcome the limits of chiral selectors by using polarized light as label-free and high-throughput chiral selectors. However, conventional chiroptical methods suffer from large sample consumption and low molar sensitivity for metabolic molecules with ultrasmall molecular mass and weak light-matter interactions, hindering their applications on detecting the trace chiral metabolites in urine.

Plasmonic chiral metamaterials with strongly enhanced chiral electromagnetic fields, also known as superchiral fields, have recently proven promising in label-free chiral sensing of biomedical molecules with significantly improved sensitivity. 12-20 The locally increased twisting of light polarization in superchiral fields can induce intense chiral light-matter interactions, causing asymmetric spectral shifts of the metamaterials upon adsorption of enantiomers, enabling ultrasensitive molecular chirality sensing. 12 Enantioselective discrimination of chiral molecules at the picogram level has been demonstrated for molecules with a wide range of molecular weights.<sup>17</sup> However, plasmon-enhanced chiral sensing requires the analytes to be physically adsorbed on the plasmonic surfaces or residing near the superchiral fields with short (nanometer-scale) working distances. Therefore, although such techniques can significantly reduce the requirement on sample consumption in comparison with conventional chiroptical methods, the lowest detectable analyte concentration in a biofluid is limited at ~1 mM to ensure sufficient molecule—metamaterial interactions, hindering the chiral sensing of trace urine metabolomes in clinical applications. To overcome the Brownian diffusion-limited biosensing, several techniques have been proposed including electrophoresis, thermophoresis, and electrothermoplasmonics. Recently, Marangoni convection induced by optothermally generated microbubbles has been used for concentrating nanoparticles and proteins, significantly enhancing the sensitivity of the biosensors. 24–26

Herein, we demonstrate microbubble-induced intense accumulation of biomolecules onto our recently developed plasmonic moiré chiral metamaterials (MCMs)<sup>27-30</sup> for chiral sensing of metabolites. Benefiting from the increased molecular occupation at the superchiral fields, we have achieved the chiral detection of a solution with glucose and lactate (dominant chiral metabolic molecules in urine) at concentrations down to 100 pM without the need for chiral selectors. The strongly enhanced sensitivity further enables the chirality determination for solutions with mixtures of various metabolic molecules, requiring only 10  $\mu$ L of samples. Finally, in combination with a simple centrifugal purification process to exclude large nonmetabolic molecules and cells from urine, as shown in Figure 1(a) and detailed in Methods, the accumulation-assisted plasmonic chiral sensing has successfully uncovered the diabetes-induced abnormal chirality in mice and human urine with a high diagnostic accuracy of 84% for human clinical samples.

## **RESULTS AND DISCUSSION**

Working Principles of Accumulation-Assisted Plasmonic Chiral Sensing. The ultrahigh sensitivity in chiral

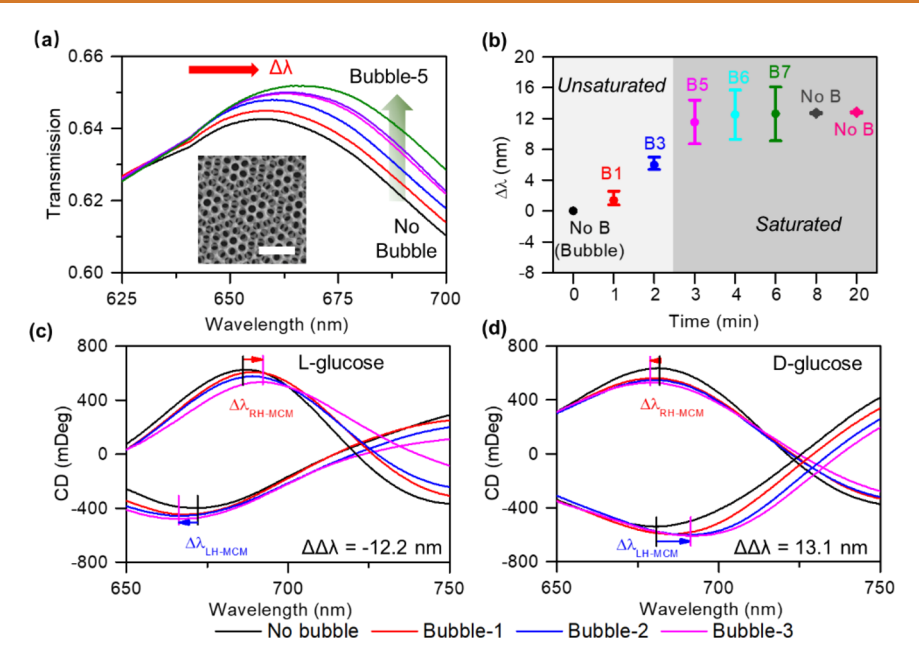


Figure 2. (a) Evolution of transmission spectra of an LH-MCM during the successive microbubble-assisted accumulation of glucose on the substrate. The inset shows the corresponding SEM images of the LH-MCM. The scale bar is 1  $\mu$ m. (b) Averaged peak shifts ( $\Delta\lambda$ ) of transmission spectra of multiple MCMs during the successive microbubble-assisted accumulation of glucose. The x axis shows the time of each measurement. (c, d) Evolution of CD spectra of LH-MCMs and RH-MCMs during the successive microbubble-assisted accumulation of (c) L- and (d) D-glucose.

sensing of biomolecules is enabled by two enhancement mechanisms, the microbubble-induced accumulation of biomolecules onto the chiral plasmonic substrates and the subsequent plasmon-enhanced chiral sensing. In this work, we apply our recently developed plasmonic MCMs, 27-30 which consist of two layers of Au nanohole arrays stacked into moiré patterns, to generate both the optothermal microbubbles and the superchiral fields. As shown in Figure 1(a), the irradiation of a focused laser onto the MCMs induces plasmon-enhanced optical heating at the laser focus point, vaporizing the solution above the substrate and generating a microbubble. The microbubble-induced Marangoni convection can effectively drag biomolecules in the solution toward the laser spot. The finite element analysis (FEM) simulation on a microbubble with a size of 5  $\mu$ m shows that the Marangoni convection dominates over natural convection by several orders of magnitude, enabling a maximum flow velocity of ~0.5 m/s near the gas/liquid interfaces (Supplementary Figure S1). We have further simulated the drag forces for randomly distributed glucose molecules near the microbubble using FEM. The acceleration can reach over 108 m/s2 near the microbubble surface for glucose molecules (Supplementary Figure S2), overcoming the limits in concentrating small biomolecules using other techniques such as electrophoresis,<sup>21</sup> thermophoretics, <sup>22</sup> and electrothermoplasmonics. <sup>23</sup> The increased concentration of molecules near the substrate and the strong downward forces at the stagnation area near the microbubblesubstrate interfaces then effectively print the molecules onto the plasmonic substrate with high binding affinity, 24,31,32 enabling effective molecule accumulation for enhanced sensitivity.<sup>33</sup> Meanwhile, the localized accumulation through microbubble concentration also benefits the durability of MCMs. Assuming an ideal MCM sample is 1 cm<sup>2</sup> in area with equal amounts of LH- and RH-MCMs and the area needed for each measurement is  $\sim$ 5  $\mu$ m<sup>2</sup>, the durability of the MCMs can

be up to millions of times. The approximated area of bubble-printed molecules is 5  $\mu$ m<sup>2</sup> on the substrate.

The plasmon-enhanced chiral near-fields further improve the chiral sensing of the accumulated molecules. We have previously demonstrated the generation of strong near-field optical chirality in the left-handed (LH) and right-handed (RH) MCMs with precisely controllable handedness through the interlayer rotation angle between the two layers of Au nanohole arrays.<sup>27-29</sup> Figure 1(b and c) show the simulated cross-sectional distribution of plasmon-enhanced electric fields for an RH-MCM with a 15° interlayer rotation angle under incident light with RH circular polarization (RCP) and LH circular polarization (LCP), respectively. The large differences in both distribution and amplitude of electric hot spots under RCP and LCP excitations show the strong chiroptical responses of the MCM. We have further simulated superchiral fields, which are quantified by the local optical chirality (C), in the MCM under LCP and RCP excitations, respectively, as shown in Figure 1(d and e). The local optical chirality (C) is obtained by  $C = -n^2 \varepsilon_0 \omega \text{ Im}[E^* \cdot B]/2$ , where n,  $\varepsilon_0$ ,  $\omega$ , E, and Bare the refractive index, free space permittivity, frequency, local electric fields, and local magnetic fields, respectively. The local optical chirality (C) is used to quantify the near-field chirality in the excitation of chiral molecules with plasmonic nanostructure. The positive sign is corresponding to LCP, while the negative sign is corresponding to RCP. 34,35 The large enhancement factors (~10) of local optical chirality enable the strongly enhanced chiral light-matter interactions and enantioselective discrimination of chiral metabolic molecules through asymmetric spectral shifts, as schematically shown in Figure  $1(a)^{12,27}$ 

We have tested the microbubble-assisted accumulation on MCMs and its effects in chiral sensing using a 100  $\mu$ M glucose solution in deionized water. Successive microbubbles are generated at the same spot, where each microbubble is maintained for 5 s and allowed to collapse before the

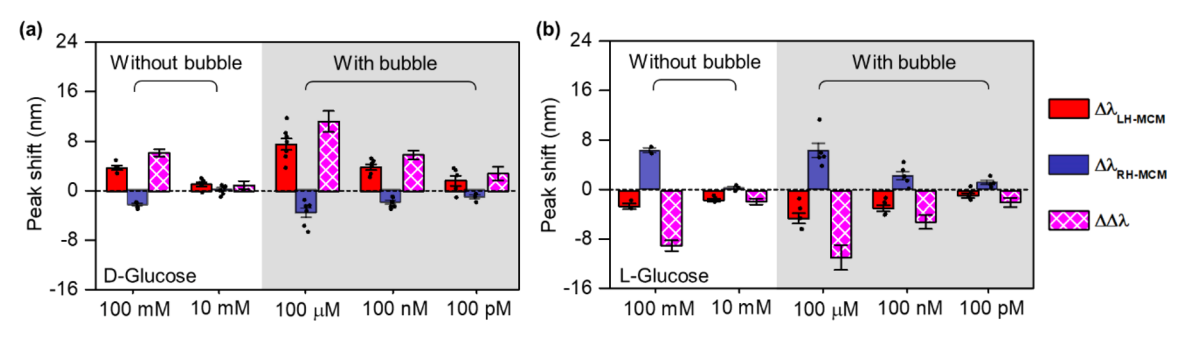


Figure 3. (a, b) CD spectral shifts ( $\Delta\lambda$ ) and dissymmetry factors ( $\Delta\Delta\lambda$ ) induced by adsorption of (a) D-glucose and (b) L-glucose, respectively, at different concentrations with and without microbubble-enabled accumulation. The bubble concentration times for 100  $\mu$ M, 100 nM, and 100 pM solutions are 5 s, 60 s, and 20 min, respectively. Error bars indicate mean  $\pm$  SD.

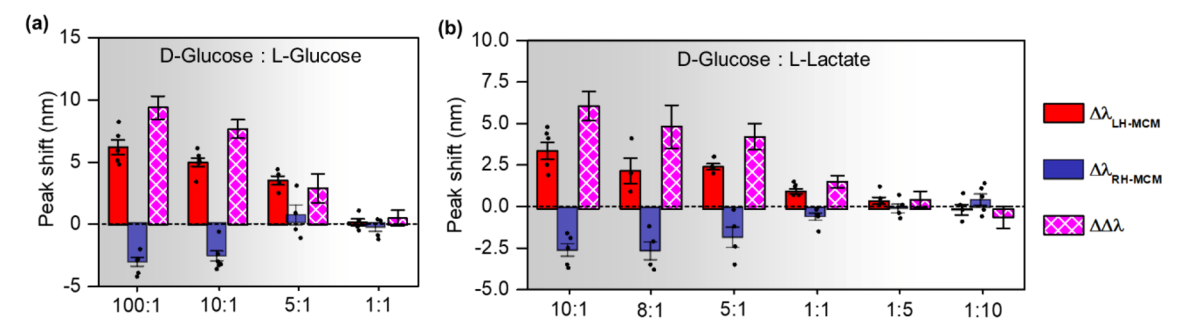


Figure 4. (a) CD spectral shifts  $(\Delta\lambda)$  and dissymmetry factors  $(\Delta\Delta\lambda)$  at various ratios of a D- and L-glucose mixture solution with 100  $\mu$ M total concentration. (b) CD spectral shifts  $(\Delta\lambda)$  and dissymmetry factors  $(\Delta\Delta\lambda)$  at various ratios of D-glucose and L-lactate mixture solutions with 100  $\mu$ M total concentration. Error bars indicate mean  $\pm$  SD. The bubble concentration time for the mixture solutions is 5 s.

generation of the next microbubble. The total time from bubble generation to collapse is within 10 s, showing several orders faster molecule accumulation than other techniques. 24,36 The optical transmission of the MCMs is measured after the collapse of each bubble. Continuous red-shifts in the transmission spectra can be observed after the successive generation of microbubbles, as shown in Figure 2(a). The spectral shifts  $(\Delta \lambda)$  are saturated at ~12 nm after 5 microbubbles and remain unchanged after more than 10 min without new microbubble generation, indicating the complete and stable occupation of plasmonic hot spots with accumulated glucose molecules. The scanning electron microscope image in Supplementary Figure S3 shows the concentrated glucose molecules on the MCM after the collapse of the microbubble, confirming that the molecules are firmly printed on the substrates. It is worth mentioning that the microbubbles are generated using optimized laser power to ensure that the local temperature is below the denaturizing point (146 °C) for glucose.37,38

The chiral sensing of the accumulated molecules is then achieved by analyzing the asymmetric shifts of the CD spectra of LH- and RH-MCMs upon the adsorption of chiral molecules. Here the CD is obtained by  $32.98^{\circ} \times (T_{\rm RCP} - T_{\rm LCP})$ , where  $T_{\rm RCP}$  and  $T_{\rm LCP}$  are the optical transmission of MCMs under RCP and LCP light, respectively. Figure 2(c) and (d) show the CD spectral shifts of the LH- and RH-MCMs induced by the successive microbubble-assisted accumulation of L- and D-glucose, respectively. The successive printing of L-glucose on the substrate causes continuous redshifts for the CD peak of the RH-MCM and continuous blueshifts for the CD dip of the RH-MCMs, as shown in Figure 2(c). In contrast, the spectral shifting trends are reversed for the D-glucose cases (*i.e.*, blue-shifts for the LH-MCM and red-

shifts for the RH-MCMs), as shown in Figure 2(d). We quantify the molecular chirality-dependent asymmetric CD spectral shifts of the MCMs using dissymmetry factors ( $\Delta\Delta\lambda$  =  $\Delta \lambda_{\text{LH-MCM}} - \Delta \lambda_{\text{RH-MCM}}$ ), where  $\Delta \lambda_{\text{LH-MCM}}$  and  $\Delta \lambda_{\text{RH-MCM}}$  are the CD spectral shifts of LH-MCM and RH-MCM, respectively, due to the microbubble-induced accumulation of chiral molecules on the MCMs. As shown in Figure 2(c and d), the successive generation of three microbubbles (completed in less than 1 min) leads to dissymmetry factors of -12.2 and 13.1 nm for a 100  $\mu$ M solution of L- and D-glucose, respectively, enabling the effective detection of molecular chirality. We have further verified the chiral sensing effectiveness of our technique by comparing the magnitudes of CD spectra of the LH- and RH-MCMs before and after molecule adsorption, <sup>17,40</sup> where asymmetric summation of CD can be generated by chiral molecules as shown in Supplementary Figure S4. To confirm that no photothermally induced chiral denaturation occurs during microbubble generation, we have measured the CD spectra of D-glucose solutions using a UV-CD spectrometer before and after a boiling water bath. The absence of spectral changes caused by the water bath indicates that the chiral parameters of glucose remain stable at water vapor generation temperature (Supplementary Figure S5).

We then demonstrated the large enhancement in sensitivity of the chiral sensing achieved by microbubble-induced accumulation. We compare the dissymmetry factors obtained by accumulation-enhanced sensing and conventional stationary sensing without microbubble generation, where the chirality detection is achieved by the comparison between CD shifts in solution with and without chiral molecules.<sup>27</sup> Figure 3 shows the sensing performances for both D- and L-glucose solution with various concentrations. For stationary sensing without

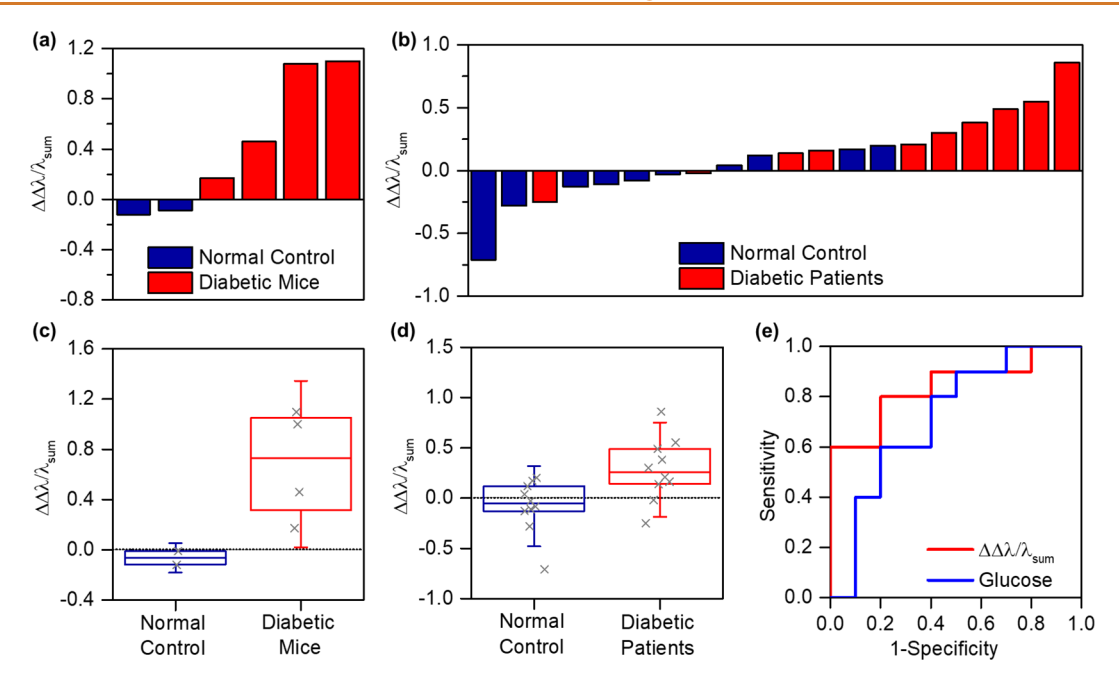


Figure 5. (a, c) Normalized dissymmetry factors  $(\Delta\Delta\lambda/\lambda_{\text{sum}})$  measured for urine samples from diabetic and normal mice. (b, d) Normalized dissymmetry factors  $(\Delta\Delta\lambda/\lambda_{\text{sum}})$  measured for urine samples from normal and diabetic humans. The median and the upper and lower quartiles are shown in the box. The whiskers represent the mean plus or minus 1.5 × SD. (e) Receiver operating characteristic curves (ROC) of  $\Delta\Delta\lambda/\lambda_{\text{sum}}$  and glucose concentration. The bubble concentration time for the urine solutions is 5 s.

microbubble-induced accumulation, the dissymmetry factors  $(\Delta\Delta\lambda)$  of both D- and L-glucose solution reduce as concentration decreases. At a concentration of 10 mM (i.e., 18 mg/mL),  $\Delta\Delta\lambda$  has a negative value of -1.8 nm for Lglucose and a positive value of 1.9 nm for D-glucose, which are comparable to the state-of-the-art superchiral-fields-enabled chiral sensing.<sup>12</sup> When glucose concentration is further reduced, the CD spectral shifts cannot be resolved using the stationary method, leading to undetectable chirality. In comparison, the microbubble-induced accumulation-enhanced sensing can achieve even larger dissymmetry factors at a glucose concentration of 100  $\mu$ M than the value obtained at 100 mM using the stationary method, as shown in Figure 3. Extraordinarily, the chirality of glucose can still be resolved when the concentration is down to 100 pM (i.e., 18 pg/mL), which shows  $\sim 10^7$  times enhancement in sensitivity comparing to state-of-the-art plasmonic chiral sensors. 12,1

Chirality Determination of Metabolite Mixtures. We have further applied the accumulation-assisted plasmonic chiral sensing in ultrasensitive monitoring chirality changes in solution with various mixtures of chiral biomolecules. Such capability is crucial in developing techniques for quantitatively monitoring the chirality of urine metabolites, which consist of enantiomers of various metabolic molecules. We first apply the accumulation-assisted plasmonic chiral sensing to determine the chirality of a solution with D- and L-glucose at various enantiomeric ratios, as shown in Figure 4(a). The dissymmetry factor  $(\Delta\Delta\lambda)$  gradually decreases from ~9 nm to ~0 nm as the ratio between D- and L-glucose decreases from 100:1 (i.e., near pure) to 1:1 (i.e., racemic), showing the good match between measured chirality via accumulation-assisted plasmonic chiral sensing and the actual enantiomeric status in solution. We have further tested the chirality monitoring of mixtures with different chiral biomolecules. As an example, we measured the dissymmetry factors of solutions with mixtures of D-glucose and L-lactate at various ratios. In a controlled experiment, we

have shown that the microbubbles have near equal accumulation efficiencies for glucose and lactate (Supplementary Figure S6). In another controlled experiment, we have also shown that the accumulation-assisted plasmonic chiral sensing can determine the chirality of a pure lactate solution with high accuracy (Supplementary Figure S7). As shown in Figure 4(b), the measured dissymmetry factor  $(\Delta \Delta \lambda)$  gradually evolves from positive to negative as the ratio of D-glucose to L-lactate increases, matching the gradual changes from dextrorotatory to levorotatory status in solution. It is worth mentioning that the measured dissymmetry factors ( $\Delta\Delta\lambda$ ) have different absolute values between the 10:1 and 1:10 (D-glucose:L-lactate) cases. In addition, in contrast to the near-zero value for the 1:1 mixture of D- and L-glucose solution, the dissymmetry factor  $(\Delta\Delta\lambda)$  shows a positive value (~1.7 nm) in a 1:1 mixture of Dglucose and L-lactate. Such differences are attributed to the different chiral parameters between glucose and lactate, where polarimeter has proven to be an alternative method to quantify the magnitude of chiral parameters (Supplementary Figure S8). Compared with commercial polarimeters, requiring sample amounts of several milliliters, our technique can achieve chirality sensing at 100  $\mu$ M using only ~10  $\mu$ L of sample, corresponding to 3 orders reduction in sample

Detection of Diabetes-Induced Abnormal Chirality. Abnormal chirality of metabolites in plasma has been measured using a polarimeter approach and has proven promising as an indicator for diabetes detection. However, sensing the chirality of metabolites in urine samples is less invasive and can be developed as a potential noninvasive point-of-care diagnosis. However, many metabolites, including glucose, are reduced by 3 orders of magnitude compared to the blood level. With the several orders of improved sensitivity of the accumulation-assisted plasmonic chiral sensor, we have overcome the detection limit of conventional polarimeters, enabling the rapid determination of total chirality of

metabolites in urine with high accuracy. We first tested the effectiveness of our technique on urine samples collected from mice with and without diabetes. The protocols for preparing, collecting, and purifying urine samples from mice are detailed in Methods. As shown in Figure 5(a) and (c) and Supplementary Figure S9, the normalized dissymmetry factors  $(\Delta\Delta\lambda/\lambda_{\text{sum}})$  measured using our accumulation-assisted plasmonic chiral sensor have average values of -0.07 and 0.7 for urine samples collected from normal and diabetic mice, respectively. Due to MCM artifacts and variation of bubble concentration efficiency between samples, we used the normalized dissymmetry factors instead of dissymmetry factors to minimize system errors. The negative value of  $\Delta\Delta\lambda/\lambda_{\text{sum}}$  for controls indicates that normal urine is dominated by LH molecules such as L-lactates, L-amino acids, and derivatives. 44 Comparing the normalized dissymmetry factors to the concentrations of glucose and lactate obtained using an enzymatic method (as shown in Supplementary Table S1), the abnormal dextrorotatory values in normalized dissymmetry factors for samples from diabetic mice could be attributed to the diabetes-induced increase of the D-glucose level in urine. The large differences in the measured normalized dissymmetry factors demonstrate the effectiveness of our accumulationassisted plasmonic chiral sensors in monitoring the chirality changes in urine metabolites. The opposite signs and small overlaps in the measured normalized dissymmetry factors also reveal the existence of diabetes-induced abnormal chirality in the urine of mice.

We then applied our accumulation-assisted plasmonic chiral sensor to urine samples collected from humans with and without diabetes. Similar to the mice, the values of normalized dissymmetry factors  $(\Delta\Delta\lambda/\lambda_{sum})$  for the diabetic samples are overall more positive than those of normal samples, as shown in Figure 5(b) and Supplementary Figures S10 and S11. We also measured the glucose and lactate concentration in both normal and diabetic human urine using an enzymatic test for comparison (Table S2 and Table S3). The level of these metabolites shows 1 order lower average values than those in mice urine (Table S1) likely due to the greater volume in human urine. Such a low level of metabolite concentration will be difficult to accurately detect with other approaches. In addition, chirality changes will also be very difficult to detect via conventional label-free chiroptical methods (i.e., CD spectrometry and polarimetry) due to the low concentration of the enantiomeric metabolites in human urine. In comparison, despite the existence of a small overlap in values, the good contrast in the normalized dissymmetry factors between normal and diabetic urine samples demonstrates the capability of our method to uncover the otherwise hidden strong correlations between diabetes and abnormal chirality of metabolites in human urine, as shown in Figure 5(d).

We further conducted receiver operating characteristic (ROC) analysis to determine the diagnostic accuracy by calculating the area under the curve (AUC) values. The AUC value obtained using the accumulation-assisted plasmonic chiral sensor based on  $\Delta\Delta\lambda/\lambda_{\rm sum}$  is 84%, as shown in Figure 5(e), demonstrating the potential value of our technique in noninvasive diagnostic applications. In comparison, the AUC value is 72% in the same cohort for enzyme tests of glucose in urine, which is a standard biomarker for conventional diabetes examination. The higher AUC value of our approach may partly be explained by the better sensitivity of glucosuria with our methods as well as detecting overall chirality from non-

glucose urine metabolites. The overall chiral changes of urine molecules could be more accurate as markers than elevated glucose concentration in urine for the screening of diabetes. As several studies have also identified an increase in D-lactate and D-amino acids in the urine of patients with diabetes and the link to diabetes-related complications, there may be added value in measuring and quantifying total urine chirality in patients with known diabetes. The higher AUC value from the chirality analysis than the urine glucose concentration alone indicates the likely abnormal changes of other chiral molecules (i.e., carboxylic acids and amino acids) besides glucose in diabetic human urine. We have selectively compared the Llactate concentrations in human urine samples between normal controls and patients with diabetes with similarly low glucose concentrations (below 1 mM) in this cohort. As shown in Figure S12, the diabetic patients in this group have lower urinary L-lactate concentrations than normal controls. Considering the well-studied increase of D-lactate in diabetes patients, 8,45-47 we hypothesize that the abnormal changes of D- to L-lactate ratio could contribute to the more dextrorotary values in total chirality in diabetic patients over normal controls in our study. Therefore, the diagnostic accuracy is improved using our technique than using enzymatic approaches for glucose, especially when controls and diabetics have similar glucose levels. It is worth noting that the abnormal levels of chiral amino acids in diabetes, which have been observed in plasma and nails but less studied in urine, could also contribute to the changes in total chirality. 6,48,49 Our results indicate the need for more studies on correlations between diabetes and abnormal chiral changes of metabolic molecules in urine. Such measurements in well-defined cohorts may be useful for a better understanding and noninvasive diagnosis of diabetes and its complications.

### **CONCLUSIONS**

In summary, we have developed accumulation-assisted plasmonic chiral sensing to achieve ultrasensitive, rapid, and label-free chirality detection of diabetes-related metabolic molecules. The optothermally generated microbubbles create strong Marangoni convections, enabling large drag forces on metabolic molecules with small molar masses toward the plasmonic chiral metamaterials. The dense occupation of accumulated molecules at the plasmonic hot spots in metamaterials enables label-free chiral detection of glucose down to 100 pM. We have further achieved the detection and monitoring of ratio-dependent chirality changes in mixtures of various metabolic molecules with high sensitivity and accuracy, while requiring 3 orders less sample consumption ( $\sim$ 10  $\mu$ L) than commercial chiroptical techniques. Benefiting from the ultrahigh sensitivity and low sample consumption, the accumulation-assisted plasmonic chiral sensing has revealed the typically hidden diabetes-induced abnormal chirality of metabolites in urine samples collected from mice and humans. The ROC analysis of our technique demonstrates a higher diagnostic accuracy of 84% in comparison with 72% from enzyme tests of glucose level for human urine samples. Our results reveal an important role of abnormal chirality of urine metabolites in future studies of patients with diabetes. The high cost-effectiveness and short characterization time (<1 min) of accumulation-assisted plasmonic chiral sensing show great potential in the development of point-of-care devices for first-line noninvasive screening and prognosis of early stage prediabetes or diabetes and its complications. We envision that

more detailed chiral analysis could be enabled using our technique by enhancing the specificity *via* improved filtering or integration of microfluidic-based separation techniques. As chiral molecules have been found to be altered in several cancers as well, a routine chiral detection that is sensitive and noninvasive could also be used for detecting occult malignancies based on human urine testing. <sup>51</sup>

## **METHODS**

Optical Setup. The experimental setup is shown in Supplementary Figure S13. The optical setup consists of an inverted microscope with a white light source. A highly focused laser beam with a wavelength of 532 nm was first expanded with a 5× beam expander to increase its beam diameter. Then the beam diameter was reduced to 5  $\mu$ m and applied to heat the MCMs for microbubble generation after an infinity-corrected tube lens (Nikon) and an objective lens. The circularly polarized light is generated by sequentially passing the broadband halogen lamp light through a linear polarizer and a quarter-wave plate. The transmission spectra of the circularly polarized light after passing through MCMs were collected with an in situ spectrometer. The tunable slit between the spectrometer and the objective is adjusted to 10  $\mu$ m to avoid background noise. A motorized microscope stage with stepper motor was used to precisely change the position of the focused laser beam in the x-y plane and align the laser at the center position on the spectrometer for each measurement. LabVIEW software was used to control the power of the laser beam for the bubble generation.

Substrate Fabrication. MCMs were fabricated on glass substrates through nanosphere lithography and wet etching/transfer as reported previously. The polystyrene spheres were purchased from Thermo Scientific Inc. The fabrication process can be divided into two processes. In process 1, the glass substrate was cleaned with acetone and deionized water and then dried with nitrogen flow. Monolayer polystyrene spheres were then self-assembled into a hexagonally closed-packed colloidal monolayer on the glass substrate. Reactive ion etching (March Plasma CS170IF RIE Etching System) was applied to reduce the diameters of the polystyrene spheres. The substrate is then coated with a chrome layer as an adhesive layer and Au layer through electron beam evaporation (Cooke ebeam/sputter deposition system). The polystyrene spheres were peeled off by the adhesive tape, leaving uniform Au nanohole arrays on the substrate.

In process 2, a sacrificial Cu layer was first deposited on the precleaned glass substrate through electron beam evaporation. The following steps are similar to those of process 1. Briefly, uniform Au nanohole arrays are fabricated on the Cu layers. Then a thin poly(methyl methacrylate) (PMMA) film is spin coated on the Au nanohole arrays, followed by baking. The selective etching of the Cu substrate was achieved by floating the substrate on the Cu etchant. The floating substrate was then transferred onto the Au nanohole arrays fabricated in process 1, followed by drying overnight in a vacuum oven at room temperature. The substrate was then dipped into an acetone solution to remove the PMMA layer, washed by deionized water, and dried under nitrogen gas. Finally, the substrate was baked on the heater to remove excess water.

Chemical and Urine Preparation. L-Glucose, D-glucose, L-lactate, and D-lactate were all purchased from Sigma-Aldrich. The solutions with various concentrations were prepared using filtered deionized water. The diabetic mice were purchased and were bred for use as type-II diabetes models. The deidentified human urine solutions were collected at clinics, prepped by centrifugation, and then aliquoted for storage at  $-80\,^{\circ}$ C. To filter large cells, extracellular vesicles, and proteins, we further centrifuged the urine samples using filters and left the remaining solution with ultrametabolites for measurement.

**Sample Preparation.** Before experiments, the MCMs were first washed using deionized water and dried with nitrogen gas, followed by oxygen plasmon cleaning in UV ozone. An adhesive spacer was firmly placed onto the MCM substrates. Next, we added a droplet of water or analytes ( $\sim$ 10  $\mu$ L) into channels on the spacer. Another

clean glass slide was then placed on top of the analyte solutions, forming a sealed microfluidic cell, which was then placed on the stage of the inverted microscope for analysis. We waited for 10 s for the liquid to stabilize and then conducted the optical characterization.

After the measurement, we removed the top glass slides and added deionized water to remove the analytes. Then we dipped the substrate into the deionized water for 5 min and dried it with nitrogen flow for the next measurement.

**Optical Characterization.** Each optical measurement was conducted using accumulated acquisition protocols to reduce the spectral noise. For each analyte, more than three measurements were conducted on LH-MCMs and RH-MCMS, respectively. Specifically, in the stationary case, the CD spectrum is first measured in deionized water without analytes and then measured with the analytes. In the accumulation-assisted concentration case, we first measured the CD spectra before the preconcentration of the analytes and then conducted the accumulation-assisted concentration at the same location. After the bubble collapses, we took another CD spectra measurement and compared it with the previous CD spectra before preconcentration. The duration of each bubble preconcentration is described in the legend of each figure. The data will be considered valid only when there is a continuous red-shift in the transmission spectra after bubble concentration.

**Enzymatic Methods.** The glucose and lactate were measured using biochemistry analyzers, which utilize the inherent specificity of enzyme reactions for multiple analyte detection through a single measurement.

**Numerical Simulations.** We used a commercially available software package (FDTD Solutions, Lumerical Inc.) to simulate the transmission spectra and near-field distributions of MCMs. The circularly polarized light was excited by the combination of an x-polarized plane-wave source with its phase set to 0 and a y-polarized plane-wave source with its phase set to +90 or -90 deg. The dielectric function of the Au was taken from Johnson and Christy. The reflective index of the surrounding medium was set to 1.33. The mesh size within the plasmonic materials was 5 nm in all three directions. The mesh size for other regions was adjusted to 10 nm. All outer boundaries were set as perfectly matched layers.

The temperature and flow simulations were performed using COMSOL Multiphysics (www.comsol.com, ver. 5.4a). A 2D axissymmetric model comprising a glass substrate and water was established. The physics of the model includes preloaded modules of heat transfer in solids, liquids, and nonisothermal laminar flow coupled with conjugate heat transfer physics. For Rayleigh Barnard convection, no bubble is modeled, and a rectangular domain was utilized with density as a function of temperature. The temperature is evaluated, density is calculated, and the flow velocity is updated in an iterative method by the solver, resulting in a converging solution. For simulating Marangoni flow, a bubble is geometrically inserted, and modules embedded within the laminar flow module are utilized to input the surface tension gradient on the bubble surface. Laser power absorbed by the gold substrate is modeled as Gaussian heat influx and is coupled to heat transfer in water using temperature continuity at the surface. The metasurfaces are incorporated into the model through the absorption coefficient fraction of the experimental laser power. Other surfaces are maintained at a room temperature of 293 K.

## **ASSOCIATED CONTENT**

#### **Supporting Information**

The Supporting Information is available free of charge at https://pubs.acs.org/doi/10.1021/acsnano.0c08822.

Figures of buoyancy-driven natural convection and Marangoni convection, acceleration of molecules, SEM image of the substrate after bubble concentration, CD summation for L- and D-glucose, CD spectra of pure glucose before and after heating, transmission spectra shift for D-glucose and L-lactate, CD spectra shift for L-/D-lactate, chiral parameter of a D-glucose and L-lactate

mixture, CD spectral shifts and dissymmetry factors of normal and diabetic mice urine, CD spectra shift and dissymmetry factor for normal and diabetes human urine, D-glucose and L-lactate concentration in the selected human groups, schematic of the experimental setup for optical measurement, tables of measured D-glucose and L-lactate concentration of normal and diabetes mice urine, D-glucose and L-lactate levels for normal and diabetic human urine (PDF)

#### **AUTHOR INFORMATION**

#### **Corresponding Authors**

Kumar Sharma – Center for Renal Precision Medicine, The University of Texas Health Science Center at San Antonio, San Antonio, Texas 78249, United States;

Email: SharmaK3@uthscsa.edu

Yuebing Zheng — Department of Electrical and Computer Engineering, Walker Department of Mechanical Engineering, Materials Science & Engineering Program and Texas Materials Institute, and Department of Biomedical Engineering, The University of Texas at Austin, Austin, Texas 78712, United States; Orcid.org/0000-0002-9168-9477; Email: zheng@austin.utexas.edu

#### Authors

Yaoran Liu — Department of Electrical and Computer Engineering, The University of Texas at Austin, Austin, Texas 78712, United States

Zilong Wu — Walker Department of Mechanical Engineering and Materials Science & Engineering Program and Texas Materials Institute, The University of Texas at Austin, Austin, Texas 78712, United States; © orcid.org/0000-0001-9323-7768

Pavana Siddhartha Kollipara — Walker Department of Mechanical Engineering, The University of Texas at Austin, Austin, Texas 78712, United States; oorcid.org/0000-0003-0166-6720

Richard Montellano – Center for Renal Precision Medicine, The University of Texas Health Science Center at San Antonio, San Antonio, Texas 78249, United States

Complete contact information is available at: https://pubs.acs.org/10.1021/acsnano.0c08822

# **Author Contributions**

<sup>#</sup>Y.L. and Z.W. contributed equally to this work.

#### **Author Contributions**

Y.L., Z.W., K.S., and Y.Z. conceived the idea. Y.L. worked on the experiments. Y.L. and Z.W. conducted the FDTD simulations. P.S.K. conducted the Comsol simulations. R.M. prepared the urine samples. K.S. and Y.Z. supervised the project. All authors participated in the discussions of the results and wrote the manuscript.

#### **Notes**

The authors declare no competing financial interest.

#### **ACKNOWLEDGMENTS**

Y.L., Z.W., P.K., and Y.Z. acknowledge the financial support of National Aeronautics and Space Administration (80NSSC17K0520), National Institute of General Medical Sciences of the National Institutes of Health (DP2GM128446), and National Science Foundation (CMMI-1761743), and R.M. and K.S. acknowledge the

financial support from University of Texas Health San Antonio. We also thank Dr. Nathaniel Lynd at the Mcketta Department of Chemical Engineering for providing optical rotation measurement and Texas Advanced Computing Centre at The University of Texas at Austin (http://www.tacc.utexas.edu) for providing HPC resources that have contributed to the research results reported within this paper.

#### REFERENCES

- (1) Cahn, R. S.; Ingold, C.; Prelog, V. Specification of Molecular Chirality. *Angew. Chem., Int. Ed. Engl.* **1966**, *5*, 385–415.
- (2) Yekkala, R.; Meers, C.; Van Schepdael, A.; Hoogmartens, J.; Lambrichts, I.; Willems, G. Racemization of Aspartic Acid From Human Dentin in the Estimation of Chronological Age. *Forensic Sci. Int.* **2006**, *159*, S89–S94.
- (3) Helfman, P. M.; BADA, J. L. Aspartic Acid Racemisation in Dentine as a Measure of Ageing. *Nature* **1976**, *262*, 279–281.
- (4) McCudden, C. R.; Kraus, V. B. Biochemistry of Amino Acid Racemization and Clinical Application to Musculoskeletal Disease. *Clin. Biochem.* **2006**, *39*, 1112–1130.
- (5) Kalíková, K.; Šlechtová, T.; Tesařová, E. Enantiomeric Ratio of Amino Acids as a Tool for Determination of Aging and Disease Diagnostics by Chromatographic Measurement. *Separations* **2016**, *3*, 30.
- (6) Kimura, T.; Hamase, K.; Miyoshi, Y.; Yamamoto, R.; Yasuda, K.; Mita, M.; Rakugi, H.; Hayashi, T.; Isaka, Y. Chiral Amino Acid Metabolomics for Novel Biomarker Screening in the Prognosis of Chronic Kidney Disease. *Sci. Rep.* **2016**, *6*, 1–7.
- (7) Murray, R. K.; Granner, D. K.; Mayes, P. A.; Rodwell, V. W. Harper's Illustrated Biochemistry; Mcgraw-Hill: New York, 2014.
- (8) Talasniemi, J. P.; Pennanen, S.; Savolainen, H.; Niskanen, L.; Liesivuori, J. Analytical Investigation: Assay of D-Lactate in Diabetic Plasma and Urine. *Clin. Biochem.* **2008**, *41*, 1099–1103.
- (9) Furusho, A.; Koga, R.; Akita, T.; Mita, M.; Kimura, T.; Hamase, K. Three-Dimensional High-Performance Liquid Chromatographic Determination of Asn, Ser, Ala, and Pro Enantiomers in the Plasma of Patients with Chronic Kidney Disease. *Anal. Chem.* **2019**, *91*, 11569–11575.
- (10) Okamoto, Y.; Ikai, T. Chiral HPLC for Efficient Resolution of Enantiomers. *Chem. Soc. Rev.* **2008**, *37*, 2593–2608.
- (11) Jiang, H. Optical MEMS for Chemical Analysis and Biomedicine; Institution of Engineering and Technology: London, 2016.
- (12) Hendry, E.; Carpy, T.; Johnston, J.; Popland, M.; Mikhaylovskiy, R.; Lapthorn, A.; Kelly, S.; Barron, L.; Gadegaard, N.; Kadodwala, M. Ultrasensitive Detection and Characterization of Biomolecules Using Superchiral Fields. *Nat. Nanotechnol.* **2010**, *5*, 783–787.
- (13) Tang, Y.; Cohen, A. E. Enhanced Enantioselectivity in Excitation of Chiral Molecules by Superchiral Light. *Science* **2011**, 332, 333–336.
- (14) Valev, V. K.; Baumberg, J. J.; Sibilia, C.; Verbiest, T. Chirality and Chiroptical Effects in Plasmonic Nanostructures: Fundamentals, Recent Progress. *Adv. Mater.* **2013**, *25*, 2517–2534.
- (15) Tullius, R.; Karimullah, A. S.; Rodier, M.; Fitzpatrick, B.; Gadegaard, N.; Barron, L. D.; Rotello, V. M.; Cooke, G.; Lapthorn, A.; Kadodwala, M. Superchiral" Spectroscopy: Detection of Protein Higher Order Hierarchical Structure With Chiral Plasmonic Nanostructures. J. Am. Chem. Soc. 2015, 137, 8380–8383.
- (16) Zhao, Y.; Belkin, M.; Alù, A. Twisted Optical Metamaterials for Planarized Ultrathin Broadband Circular Polarizers. *Nat. Commun.* **2012**, 3, 1–7.
- (17) Zhao, Y.; Askarpour, A. N.; Sun, L.; Shi, J.; Li, X.; Alù, A. Chirality Detection of Enantiomers Using Twisted Optical Metamaterials. *Nat. Commun.* **2017**, *8*, 1–8.
- (18) Rocks, L.; Faulds, K.; Graham, D.; Parchaňský, V.; Bouř, P.; Blanch, E. W. Through-Space Transfer of Chiral Information Mediated by a Plasmonic Nanomaterial. *Nat. Chem.* **2015**, *7*, 591–596.

- (19) Ong, T. T.; Blanch, E. W.; Jones, O. A. Surface Enhanced Raman Spectroscopy in Environmental Analysis. *Sci. Total Environ.* **2020**, 720, 137601.
- (20) Wei, X.; Liu, J.; Xia, G.-J.; Deng, J.; Sun, P.; Chruma, J. J.; Wu, W.; Yang, C.; Wang, Y.-G.; Huang, Z. Enantioselective Photoinduced Cyclodimerization of a Prochiral Anthracene Derivative Adsorbed on Helical Metal Nanostructures. *Nat. Chem.* **2020**, *12*, 551–559.
- (21) Lapizco-Encinas, B. H.; Simmons, B. A.; Cummings, E. B.; Fintschenko, Y. Dielectrophoretic Concentration and Separation of Live and Dead Bacteria in an Array of Insulators. *Anal. Chem.* **2004**, 76, 1571–1579.
- (22) Schermer, R. T.; Olson, C. C.; Coleman, J. P.; Bucholtz, F. Laser-Induced Thermophoresis of Individual Particles in a Viscous Liquid. *Opt. Express* **2011**, *19*, 10571–10586.
- (23) Garcia-Guirado, J.; Rica, R. A.; Ortega, J.; Medina, J.; Sanz, V.; Ruiz-Reina, E.; Quidant, R. Overcoming Diffusion-Limited Biosensing by Electrothermoplasmonics. *ACS Photonics* **2018**, *5*, 3673–3679.
- (24) Lin, L.; Peng, X.; Mao, Z.; Li, W.; Yogeesh, M. N.; Rajeeva, B. B.; Perillo, E. P.; Dunn, A. K.; Akinwande, D.; Zheng, Y. Bubble-Pen Lithography. *Nano Lett.* **2016**, *16*, 701–708.
- (25) Kotnala, A.; Kollipara, P. S.; Li, J.; Zheng, Y. Overcoming Diffusion-Limited Trapping in Nanoaperture Tweezers Using Opto-Thermal-Induced Flow. *Nano Lett.* **2020**, *20*, 768–779.
- (26) Kim, Y.; Ding, H.; Zheng, Y. Enhancing Surface Capture and Sensing of Proteins With Low-Power Optothermal Bubbles in a Biphasic Liquid. *Nano Lett.* **2020**, *20*, 7020–7027.
- (27) Wu, Z.; Zheng, Y. Moiré Chiral Metamaterials. *Adv. Opt. Mater.* **2017**, *5*, 1700034.
- (28) Wu, Z.; Zheng, Y. Moiré Metamaterials and Metasurfaces. Adv. Opt. Mater. 2018, 6, 1701057.
- (29) Wu, Z.; Liu, Y.; Hill, E. H.; Zheng, Y. Chiral Metamaterials via Moiré Stacking. Nanoscale 2018, 10, 18096–18112.
- (30) Wu, Z.; Kelp, G.; Yogeesh, M. N.; Li, W.; McNicholas, K. M.; Briggs, A.; Rajeeva, B. B.; Akinwande, D.; Bank, S. R.; Shvets, G. Dual-Band Moiré Metasurface Patches for Multifunctional Biomedical Applications. *Nanoscale* **2016**, *8*, 18461–18468.
- (31) Morasch, M.; Liu, J.; Dirscherl, C. F.; Ianeselli, A.; Kühnlein, A.; Le Vay, K.; Schwintek, P.; Islam, S.; Corpinot, M. K.; Scheu, B. Heated Gas Bubbles Enrich, Crystallize, Dry, Phosphorylate and Encapsulate Prebiotic Molecules. *Nat. Chem.* **2019**, *11*, 779–788.
- (32) Zhao, C.; Xie, Y.; Mao, Z.; Zhao, Y.; Rufo, J.; Yang, S.; Guo, F.; Mai, J. D.; Huang, T. J. Theory and Experiment on Particle Trapping and Manipulation *via* Optothermally Generated Bubbles. *Lab Chip* **2014**, *14*, 384–391.
- (33) Cheng, D.; Jiang, H. A Debubbler for Microfluidics Utilizing Air-Liquid Interfaces. *Appl. Phys. Lett.* **2009**, *95*, 214103.
- (34) Schäferling, M.; Dregely, D.; Hentschel, M.; Giessen, H. Tailoring Enhanced Optical Chirality: Design Principles for Chiral Plasmonic Nanostructures. *Phys. Rev. X* **2012**, *2*, No. 031010.
- (35) Fan, Z.; Govorov, A. O. Plasmonic Circular Dichroism of Chiral Metal Nanoparticle Assemblies. *Nano Lett.* **2010**, *10*, 2580–2587.
- (36) Karim, F.; Vasquez, E. S.; Sun, Y.; Zhao, C. Optothermal Microbubble Assisted Manufacturing of Nanogap-Rich Structures for Active Chemical Sensing. *Nanoscale* **2019**, *11*, 20589–20597.
- (37) Hurtta, M.; Pitkänen, I.; Knuutinen, J. Melting Behaviour of D-Sucrose, D-Glucose and D-Fructose. *Carbohydr. Res.* **2004**, 339, 2267–2273.
- (38) Pazur, J. H.; Kleppe, K. The Oxidation of Glucose and Related Compounds by Glucose Oxidase From Aspergillus Niger. *Biochemistry* **1964**, *3*, 578–583.
- (39) Johnson, W. C., Jr Secondary Structure of Proteins Through Circular Dichroism Spectroscopy. *Annu. Rev. Biophys. Biophys. Chem.* **1988**, *17*, 145–166.
- (40) García-Guirado, J.; Svedendahl, M.; Puigdollers, J.; Quidant, R. Enantiomer-Selective Molecular Sensing Using Racemic Nanoplasmonic Arrays. *Nano Lett.* **2018**, *18*, 6279–6285.
- (41) Pirnstill, C. W.; Malik, B. H.; Gresham, V. C.; Coté, G. L. in Vivo Glucose Monitoring Using Dual-Wavelength Polarimetry to

- Overcome Corneal Birefringence in the Presence of Motion. *Diabetes Technol. Ther.* **2012**, *14*, 819–827.
- (42) Purvinis, G.; Cameron, B. D.; Altrogge, D. M. Noninvasive Polarimetric-Based Glucose Monitoring: An *in Vivo* Study. *J. Diabetes Sci. Technol.* **2011**, *5*, 380–387.
- (43) Xu, W.; Fu, K.; Bohn, P. W. Electrochromic Sensor for Multiplex Detection of Metabolites Enabled by Closed Bipolar Electrode Coupling. *ACS Sens.* **2017**, *2*, 1020–1026.
- (44) Bouatra, S.; Aziat, F.; Mandal, R.; Guo, A. C.; Wilson, M. R.; Knox, C.; Bjorndahl, T. C.; Krishnamurthy, R.; Saleem, F.; Liu, P. The Human Urine Metabolome. *PLoS One* **2013**, *8*, No. e73076.
- (45) Christopher, M. M.; Broussard, J. D.; Fallin, C. W.; Drost, N. J.; Peterson, M. E. Increased Serum D-Lactate Associated With Diabetic Ketoacidosis. *Metab.*, *Clin. Exp.* **1995**, *44*, 287–290.
- (46) Chou, C.-K.; Lee, Y.-T.; Chen, S.-M.; Hsieh, C.-W.; Huang, T.-C.; Li, Y.-C.; Lee, J.-A. Elevated Urinary D-Lactate Levels in Patients With Diabetes and Microalbuminuria. *J. Pharm. Biomed. Anal.* **2015**, 116, 65–70.
- (47) Kondoh, Y.; Kawase, M.; Kawakami, Y.; Ohmori, S. Concentrations of D-Lactate and Its Related Metabolic Intermediates in Liver, Blood, and Muscle of Diabetic and Starved Rats. *Res. Exp. Med.* **1992**, 192, 407–414.
- (48) Lorenzo, M. P.; Dudzik, D.; Varas, E.; Gibellini, M.; Skotnicki, M.; Zorawski, M.; Zarzycki, W.; Pellati, F.; García, A. Optimization and Validation of a Chiral GC–MS Method for the Determination of Free D-Amino Acids Ratio in Human Urine: Application to a Gestational Diabetes Mellitus Study. *J. Pharm. Biomed. Anal.* 2015, 107, 480–487.
- (49) Min, J. Z.; Hatanaka, S.; Yu, H.-f.; Higashi, T.; Inagaki, S.; Toyo'oka, T. Determination of Dl-Amino Acids, Derivatized with R(-)-4-(3-Isothiocyanatopyrrolidin-1-Yl)-7-(N,N-Dimethylaminosulfonyl)-2,1,3-Benzoxadiazole in Nail of Diabetic Patients by UPLC–ESI-TOF-MS. J. Chromatogr. B: Anal. Technol. Biomed. Life Sci. 2011, 879, 3220–3228.
- (50) Hamase, K.; Morikawa, A.; Zaitsu, K. D-Amino Acids in Mammals and Their Diagnostic Value. *J. Chromatogr. B: Anal. Technol. Biomed. Life Sci.* **2002**, 781, 73–91.
- (51) Bitbol, M.; Devaux, P. F. Measurement of Outward Translocation of Phospholipids Across Human Erythrocyte Membrane. *Proc. Natl. Acad. Sci. U. S. A.* **1988**, *85*, *6783*–*6787*.
- (52) Olmon, R. L.; Slovick, B.; Johnson, T. W.; Shelton, D.; Oh, S.-H.; Boreman, G. D.; Raschke, M. B. Optical Dielectric Function of Gold. *Phys. Rev. B: Condens. Matter Mater. Phys.* **2012**, *86*, 235147.